IOP Publishing Smart Materials and Structures
Smart Mater. Struct. **26** (2017) 055029 (10pp) https://doi.org/10.1088/1361-665X/aa6671

An investigation of electroelastic bandgap formation in locally resonant piezoelectric metastructures

C Sugino[1], S Leadenham[1], M Ruzzene[1,2] and A Erturk[1]

[1] G.W. Woodruff School of Mechanical Engineering, Georgia Institute of Technology, Atlanta, GA, United States of America
[2] D. Guggenheim School of Aerospace Engineering, Georgia Institute of Technology, Atlanta, GA, United States of America

E-mail: alper.erturk@me.gatech.edu

Received 23 December 2016, revised 23 February 2017
Accepted for publication 13 March 2017
Published 19 April 2017

Abstract

Locally resonant electromechanical metastructures made from flexible substrates with piezoelectric layers connected to resonant shunt circuits exhibit vibration attenuation properties similar to those of purely mechanical metastructures. Thus, in analogy, these locally resonant electromechanical metastructures can exhibit electroelastic bandgaps at wavelengths much larger than the lattice size. In order to effectively design such metastructures, the modal behavior of the finite structure with given boundary conditions must be reconciled with the electromechanical behavior of the piezoelectric layers and shunt circuits. To this end, we develop the theory for a piezoelectric bimorph beam with segmented electrodes under transverse vibrations, and extract analytical results for bandgap estimation using modal analysis. Under the assumption of an infinite number of segmented electrodes, the locally resonant bandgap is estimated in closed form and shown to depend only on the target frequency and the system-level electromechanical coupling. It is shown that bandgap formation in piezoelectric metastructures is associated with a frequency-dependent modal stiffness, unlike the frequency-dependent modal mass in mechanical metastructures. The relevant electromechanical coupling term and the normalized bandgap size are calculated for a representative structure and a selection of piezoelectric ceramics and single crystals, revealing that single crystals (e.g. PMN-PT) result in significantly wider bandgap than ceramics (e.g. PZT-5A). Numerical studies are performed to demonstrate that the closed-form bandgap expression derived in this work holds for a finite number of electrode segments. It is shown that the number of electrodes required to create the bandgap increases as the target frequency is increased.

Keywords: metamaterials, metastructures, piezoelectricity, vibration, bandgap, damping, electromechanical

(Some figures may appear in colour only in the online journal)

1. Introduction

Piezoelectric shunt damping has been studied for many years as an effective way to reduce structural vibrations of lightweight and flexible structures without significant mass addition, one of the typical problems with conventional, purely mechanical damping techniques [1, 2]. Using piezoelectricity, energy is transferred from the mechanical to electrical domain, where it can be dissipated or stored [3, 4]. This introduces significant design freedom, since electrical energy can be manipulated by any combination of commonly available analog and digital electrical components. Forward [5] first proposed shunt damping using negative feedback and two piezoelectric patches, one acting as a sensor and the other as actuator. Hagood and von Flotow [6] showed that a single piezoelectric patch using an inductive shunt circuit acts as a

mechanical resonator, yielding an electromechanical version of the well-known dynamic vibratrion absorber effect [7]. Others have demonstrated multi-modal damping performance using more complex networks of resonant circuits [8, 9], or used negative capacitance shunting to achieve vibration reduction [10–12]. Various nonlinear switching circuits have also been shown to be effective for vibration reduction [14–16], although they introduce additional complexity.

More recently, shunt damping techniques have been employed in conjunction with locally resonant metamaterial concepts, using many piezoelectric elements on a structure to create bandgaps, or frequency ranges in which vibration disturbances will not propagate through the structure. In analogy with structures using many mechanical resonators [17, 18], structures employing many resonant shunt circuits can display 'locally resonant' bandgaps at wavelengths much larger than the lattice size [19–23], enabling the formation of low-frequency bandgaps in structures for wideband vibration and/or sound attenuation.

Typical approaches for modeling metamaterials assume an infinite or a semi-infinite structure made from a repeated unit cell, allowing the use of the Bloch theorem to obtain the band structure of the material. However, for practical implementation, it is necessary to understand the performance of finite size metamaterial-based electromechanical structures, i.e. *electromechanical metastructures*, and how the mode shapes of the structure interact with the shunt circuits. To this end, we present a distributed-parameter electromechanical model and modal analysis of a one-dimensional locally resonant thin metastructure under transverse vibrations. First the generalized segmented electrode formulation is reviewed for a finite number of shunts. Then, based on the assumption of an infinite number of segmented electrodes, the response of the beam is derived in closed form, and it is shown that the shunt circuitry admittance adds frequency-dependence to the stiffness of the structure. By assuming ideal resonant shunting, with each circuit tuned to the same resonant frequency, the locally resonant bandgap edge frequencies are derived in closed form. The bandgap edge frequencies depend only on the resonant frequency of the shunt circuits and the system-level electromechanical coupling. The coupling parameter depends on the geometry of the bimorph and the properties of the piezoelectric layers. For comparison, the expected electromechanical coupling is calculated for a variety of piezoelectric ceramics and single crystals. Numerical studies are performed for a bimorph cantilever with a finite number of segmented electrodes to validate the analytical bandgap estimation.

2. Modal analysis of electroelastic bandgap formation

Consider a bimorph piezoelectric beam with rectangular cross section made from two continuous and symmetrically located piezoelectric layers sandwiching a central structural (i.e. shim or substrate) layer (figure 1). The piezoelectric layers are oppositely poled in thickness direction and the inner

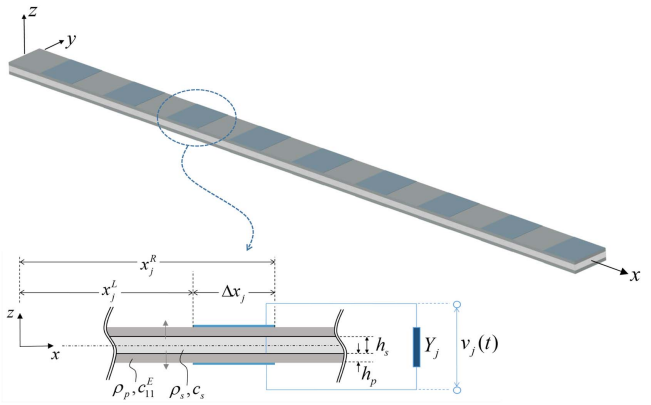

Figure 1. Schematic of a piezoelectric metastructure and a close up showing the *j*th electrode pair shunted to an electrical load of admittance Y_j. Since periodicity is not required, the electrode pairs do not have to be identical. Symmetrically located piezoelectric layers are connected in series for transvervse vibrations (poling directions are shown by gray arrows).

electrodes are combined with each other (through the conductive substrate), yielding series connection under transverse vibrations, while parallel connection is also possible by properly insulating and combining the respective electrodes. The outer surface electrodes are segmented as pairs and connected to a total of S shunt circuits. The electrode layers and the bonding layers are assumed to have negligible thickness. The thin composite beam has certain specified boundary conditions and is modeled based on the Euler–Bernoulli beam theory by assuming geometrically small oscillations and linear-elastic material behavior. For simplicity, the beam is assumed to be undamped, with the understanding that modal damping can be added easily.

Under the excitation of a distributed transverse force per unit length $f(x, t)$ (acting in z-direction in the xz-plane), the governing electromechanical equations for linear bending vibrations of the beam and current balance in shunt circuits are

$$EI\frac{\partial^4 w}{\partial x^4} + m\frac{\partial^2 w}{\partial t^2} - \vartheta\sum_{j=1}^{S} v_j(t)\frac{\mathrm{d}^2}{\mathrm{d}x^2} \times [H(x - x_j^L) - H(x - x_j^R)] = f(x, t), \tag{1}$$

$$C_{p,j}\frac{\mathrm{d}v_j}{\mathrm{d}t} + Y_j v_j(t) + \vartheta\int_{x_j^L}^{x_j^R}\frac{\partial^3 w}{\partial x^2 \partial t}\mathrm{d}x = 0, \quad j = 1,\ldots,S, \tag{2}$$

where $w(x, t)$ is the transverse displacement of the beam at position x and time t; $v_j(t)$ and Y_j are, respectively, the voltage and the external load admittance across the jth electrode pair, and $H(x)$ is the Heaviside function. Furthermore, EI is the short-circuit flexural rigidity, m is the mass per length, ϑ is the electromechanical coupling term in physical coordinates, and $C_{p,j}$ is the internal piezoelectric capacitance across the jth electrode pair, given by

$$EI = \frac{2b}{3}\left(c_s\frac{h_s^3}{8} + \bar{c}_{11}^E\left[\left(h_p + \frac{h_s}{2}\right)^3 - \frac{h_s^3}{8}\right]\right), \tag{3}$$

$$m = b(\rho_s h_s + 2\rho_p h_p), \tag{4}$$

$$\vartheta = \frac{\bar{e}_{31} b_e}{2h_p}\left[\left(h_p + \frac{h_s}{2}\right)^2 - \frac{h_s^2}{4}\right], \tag{5}$$

$$C_{p,j} = \bar{\varepsilon}_{33}^S b_e \frac{(x_j^R - x_j^L)}{2h_p}. \tag{6}$$

Here, c_s, ρ_s, and h_s are the central substrate layer's elastic modulus, mass density, and thickness, respectively, while b is the width of the beam. The piezoelectric layers have mass density ρ_p, thickness h_p, width b, elastic modulus at constant electric field $\bar{c}_{11}^E$, effective piezoelectric stress constant $\bar{e}_{31}$, and permittivity component at constant strain $\bar{\varepsilon}_{33}^S$, where the overbars indicate effective material properties for 1D thin layers reduced from 3D constitutive equations as

$$\bar{c}_{11}^E = \frac{1}{s_{11}^E}, \quad \bar{e}_{31} = \frac{d_{31}}{s_{11}^E}, \quad \bar{\varepsilon}_{33}^S = \varepsilon_{33}^T - \frac{d_{31}^2}{s_{11}^E}, \tag{7}$$

where s_{11}^E is the elastic compliance at constant electric field, d_{31} is the piezoelectric strain constant, and ε_{33}^T is the permittivity component at constant strain. The piezoelectric layers have segmented surface electrodes numbered $j = 1 \ldots S$, with each electrode starting at $x = x_j^L$ and ending at x_j^R, with total length $\Delta x_j = x_j^R - x_j^L$ (figure 1), and width b_e, symmetric about the xz-plane.

Using an assumed-modes type expansion with N number of modes, the transverse displacement of the beam can be given by

$$w(x, t) = \sum_{r=1}^{N} \phi_r(x)\eta_r(t), \tag{8}$$

where $\eta_r(t)$ are the modal weightings to be determined. The mode shapes $\phi_r(x)$ of the beam obtained for a given set of mechanical boundary conditions (at short circuit) are normalized such that

$$\int_0^L m\phi_r(x)\phi_s(x) = \delta_{rs}, \quad r, s = 1, 2, \ldots, \tag{9}$$

$$\int_0^L EI\phi_r(x)\frac{\mathrm{d}^4\phi_s}{\mathrm{d}x^4}\mathrm{d}x = \omega_r^2\delta_{rs}, \quad r, s = 1, 2, \ldots, \tag{10}$$

where L is the length of the beam, ω_r is the rth natural frequency, and δ_{rs} is the Kronecker delta. Note that equation (10) can be written in symmetric form

$$\int_0^L EI\frac{\mathrm{d}^2\phi_r}{\mathrm{d}x^2}\frac{\mathrm{d}^2\phi_s}{\mathrm{d}x^2}\mathrm{d}x = \omega_r^2\delta_{rs}, \quad r, s = 1, 2, \ldots. \tag{11}$$

Substituting equation (8) into equation (1), multiplying by some mode shape $\phi_k(x)$, and integrating across the beam (see [24] for a full derivation with a single electrode, which can be easily extended to multiple electrodes), governing equations can be obtained in modal coordinates as

$$\ddot{\eta}_r(t) + \omega_r^2\eta_r(t) - \vartheta\sum_{j=1}^{S} v_j(t)\Delta\phi'_{r,j} = q_r(t), \tag{12}$$

$$C_{p,j}\dot{v}_j(t) + Y_j v_j(t) + \vartheta\sum_{r=1}^{N}\Delta\phi'_{r,j}\dot{\eta}_r(t) = 0, \tag{13}$$

where the free indices r and j are assumed to go from 1 … N and 1 … S, respectively,

$$\Delta\phi'_{r,j} = \left(\frac{\mathrm{d}\phi_r}{\mathrm{d}x}\right)_{x_j^L}^{x_j^R} = \frac{\mathrm{d}\phi_r}{\mathrm{d}x}(x_j^R) - \frac{\mathrm{d}\phi_r}{\mathrm{d}x}(x_j^L) \tag{14}$$

is the difference in slope of the rth mode between the ends of the jth electrode and

$$q_r(t) = \int_0^L f(x, t)\phi_r(x)\mathrm{d}x \tag{15}$$

is the modal forcing. Taking the Laplace transforms of equations (12) and (13), we can obtain separate equations governing the modal weightings and voltages,

$$(s^2 + \omega_r^2)H_r(s) + s\vartheta^2\sum_{j=1}^{S}\frac{\Delta\phi'_{r,j}}{sC_{p,j} + Y_j(s)} \times \sum_{k=1}^{N}\Delta\phi'_{k,j}H_k(s) = Q_r(s), \tag{16}$$

$$(sC_{p,j} + Y_j(s))V_j(s) + s\vartheta^2\sum_{r=1}^{N}\frac{\Delta\phi'_{r,j}}{s^2 + \omega_r^2} \times \sum_{k=1}^{S}\Delta\phi'_{r,k}V_k(s) = Q_j(s). \tag{17}$$

Focusing on the modal weightings, equation (16) can be written as

$$(s^2 + \omega_r^2)H_r(s) + \frac{\alpha s}{s + h(s)}\sum_{j=1}^{S} EI\frac{\Delta\phi'_{r,j}}{\Delta x_j} \times \sum_{k=1}^{N}\frac{\Delta\phi'_{k,j}}{\Delta x_j}\Delta x_j H_k(s) = Q_r(s), \tag{18}$$

where

$$\alpha = \frac{2\vartheta^2 h_p}{EI\bar{\varepsilon}_{33}^S b_e} = \frac{\bar{e}_{31}^2 b_e h_p (h_s + h_p)^2}{2EI\bar{\varepsilon}_{33}^S} \tag{19}$$

is a dimensionless parameter related to the electromechanical coupling, and

$$h(s) = \frac{Y_j(s)}{C_{p,j}} \tag{20}$$

is the normalized circuit admittance, which is assumed to be identical for every electrode pair. The system of equations described by equation (18) cannot be readily solved for a simple analytical expression for the modal weightings $H_r(s)$ due to the coupling from the presence of the segmented electrodes (a matrix inversion solution is suitable in the generalized segmented electrode case). However, as an electrode pair becomes infinitesimally long,

$$\lim_{\Delta x_j \to 0}\frac{\Delta\phi'_{r,j}}{\Delta x_j} = \frac{\mathrm{d}^2\phi_r}{\mathrm{d}x^2}(x_j), \tag{21}$$

where $x_j = x_j^L = x_j^R$ is the x-coordinate of the infinitesimal electrode. In the limit as all of the electrodes become infinitesimal and as $S \to \infty$,

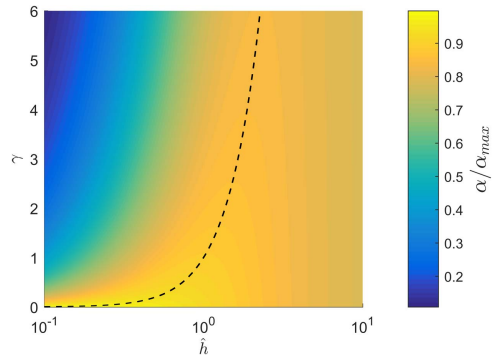

Figure 2. Dimensionless electromechanical coupling α normalized by its maximum value versus normalized piezoelectric thickness $\hat{h}$ and stiffness ratio γ. The dashed line shows the location of the maximum value of α for a given $\hat{h}$ or γ value.

$$\lim_{S\to\infty}\lim_{\Delta x_j\to 0}\sum_{j=1}^{S} EI\frac{\Delta\phi'_{r,j}}{\Delta x_j}\sum_{k=1}^{N}\frac{\Delta\phi'_{k,j}}{\Delta x_j}\Delta x_j H_k(s) = \int_0^L EI\frac{\mathrm{d}^2\phi_r}{\mathrm{d}x^2}\sum_{k=1}^{N}\frac{\mathrm{d}^2\phi_k}{\mathrm{d}x^2}\mathrm{d}x H_k(s) = \omega_r^2 H_r(s). \tag{22}$$

Although this simplification is only exact in the limiting case, it can serve as a good approximation for a finite number of electrodes, as will be discussed in later. Equation (18) then becomes

$$(s^2+\omega_r^2)H_r(s) + \frac{\alpha s}{s+h(s)}\omega_r^2 H_r(s) = Q_r(s). \tag{23}$$

Since the system of equations is now decoupled, the modal response can be explicitly calculated as

$$H_r(s) = \frac{Q_r(s)}{s^2+\omega_r^2\left(1+\frac{\alpha s}{s+h(s)}\right)}. \tag{24}$$

From this analysis, it is clear that the presence of the piezoelectric material and segmented electrodes with identical circuitry results in a frequency-dependent dynamic modal stiffness, given by

$$\frac{K(s)}{K_{SC}} = 1 + \frac{\alpha s}{s+h(s)}, \tag{25}$$

where K_{SC} is the modal stiffness of the system at short circuit. This is fundamentally different from the purely mechanical locally resonant counterparts, which results in a frequency dependent dynamic modal mass [18]. Furthermore, whereas with mechanical resonators the type of expected frequency dependence is limited to various combinations of mass-spring-damper systems, $h(s)$ is associated with the shunt circuit impedance, which greatly expands the design space, e.g. by using generalized synthetic impedance circuits via digital signal processing [25].

3. Electromechanical coupling

The key dimensionless parameter α emerges from this analysis, which measures how strongly coupled the piezoelectric material is to the plain beam, directly affecting how strongly the shunt circuitry is able to affect the structure. To gain more intuition on what material properties influence α, substituting equation (3) into equation (19) yields

$$\alpha = \frac{6b_e\bar{e}_{31}^2 h_p(h_p+h_s)^2}{b\bar{\varepsilon}_{33}^S(c_s h_s^3 + 2\bar{c}_{11}^E h_p(4h_p^2+6h_p h_s+3h_s^2))}. \tag{26}$$

Define the dimensionless parameters

$$\hat{h} = \frac{h_p}{h_s}, \quad \hat{b} = \frac{b_e}{b}, \quad \gamma = \frac{c_s}{\bar{c}_{11}^E}, \quad \beta = \frac{\bar{e}_{31}^2}{\bar{c}_{11}^E\bar{\varepsilon}_{33}^S}. \tag{27}$$

Then,

$$\alpha = \frac{6\hat{b}\beta\hat{h}(\hat{h}+1)^2}{\gamma + 2\hat{h}(4\hat{h}^2+6\hat{h}+3)}. \tag{28}$$

The coupling increases with the width of the electrodes and the material parameter β. The maximum value of α, assuming fixed β and $\hat{b}$, depends only on $\hat{h}$, given by

$$\alpha_{\max}(\hat{h}) = \frac{\hat{b}\beta(1+\hat{h})(1+3\hat{h})}{(1+2\hat{h})^2} \tag{29}$$

which occurs at $\gamma = 4\hat{h}^3/(1+3\hat{h})$ (these expressions can be rearranged to find the optimal $\hat{h}$ at a certain γ, and equivalently $\alpha_{\max}(\gamma)$). Thus, the maximum value across the entire parameter space is

$$\alpha_{\max} = \beta = \frac{\bar{e}_{31}^2}{\bar{c}_{11}^E\bar{\varepsilon}_{33}^S} = \frac{k_{31}^2}{1-k_{31}^2}, \tag{30}$$

where

$$k_{31}^2 = \frac{d_{31}^2}{s_{11}^E\varepsilon_{33}^T} \tag{31}$$

is the standard definition for the piezoelectric material's electromechanical coupling coefficient. The electromechanical coupling α is plotted against $\hat{h}$ and γ in figure 2, along with $\hat{h}$–γ combinations (dashed line) for which α is a maximum. For a fixed piezoelectric material and electrode width, the dashed line in figure 2 can therefore be used to select the optimal thickness ratio given the elastic moduli ratio, or vice versa.

In order to give a sense of the typical values of α, consider a bimorph cantilever with an aluminum substrate, with $h_s = 0.1$ mm, $c_s = 69$ GPa, $\rho_s = 2700$ kg m^{-3}, $L = 100$ mm, and $b = 10$ mm. For the piezoelectric layers, we will consider a representative set of piezoelectric materials, all with $h_p = 0.3$ mm and $b_e = b = 10$ mm. The relevant material properties and corresponding dimensionless parameters for the different piezoelectric materials are shown in table 1. Single crystals are also included in this analysis due to their significantly larger electromechanical coupling and elastic compliance. PZT-5A and PZT-5H are both commonly used piezoelectric ceramics, whereas PZN-PT, PMN-PT, and PIN-PMN-PT are single crystals. Regarding the single crystals, the table contians PZN-PT and PMN-PT data for various % content of PT, while the PIN-PMN-PT considered here has the composition of 27% PIN, 40% PMN, and 33% PT [26–28]. Since the single crystals have

Table 1. Typical properties for selected piezoelectric ceramic and single crystal materials [26–28] and corresponding dimensionless parameters defined in this work (for $c_s = 69$ GPa, $\rho_s = 2700$ kg m^{-3}, $h_s = 0.1$ mm, $h_p = 0.3$ mm, $L = 100$ mm, and $b = b_e = 10$ mm).

Material	ρ_s (kg m^{-3})	$\bar{c}_{11}^E$ (GPa)	$\bar{e}_{31}$ (C m^{-2})	ϵ_{33}^S (nF m^{-1})	β	γ	α
PZT-5A	7750	61	−12.3	13.3	0.19	1.13	0.16
PZT-5H	7500	60.6	−16.6	25.6	0.18	1.14	0.15
PZN-PT (4.5% PT)	8310	12.2	−11.8	34.6	0.33	5.65	0.27
PZN-PT (8% PT)	8315	11.5	−16.7	43.8	0.56	5.99	0.46
PMN-PT (30% PT)	8040	19.2	−17.7	52.7	0.31	3.58	0.26
PMN-PT (33% PT)	8060	14.5	−19.3	47.0	0.55	4.75	0.45
PIN-PMN-PT	8198	13.2	−17.7	40.5	0.59	5.20	0.49

lower elastic moduli and higher coupling coefficient than the piezoceramics, they give much larger values of α.

The electromechanical coupling α is also related to the amount of stiffness gained at open circuit, which can be seen simply by setting $h(s) = 0$, yielding

$$\frac{K(s)}{K_{SC}} = 1 + \alpha \tag{32}$$

indicating that the effective modal stiffness is increased by a factor of $1 + \alpha$ from short circuit to open circuit. This provides a simple way to estimate α by using

$$\alpha = \left(\frac{\omega_{OC,i}}{\omega_{SC,i}}\right)^2 - 1, \tag{33}$$

where $\omega_{OC,i}$ and $\omega_{SC,i}$ are the ith natural frequencies at open and short circuit, respectively (which roughly are the ith open- and short-circuit resonant frequencies in a typical lightly damped system). Therefore, α is related to the coupling coefficient of the *system*, i.e. the overall composite structure (which should not be confused with the coupling coefficient of the active *material* alone, given by equation (31)). A dynamic definition of the system-level electromechanical coupling coefficient k_i for the ith mode is [29]

$$k_i^2 = \frac{\omega_{OC,i}^2 - \omega_{SC,i}^2}{\omega_{OC,i}^2} \tag{34}$$

which generally depends on the mode under consideration and the electrode configuration. Using the approximation of an infinite number of electrodes, the coupling coefficient becomes the same for every mode, given by

$$k_\infty^2 = \frac{\alpha}{1 + \alpha}. \tag{35}$$

It is useful to note that, substituting the maximum value α_{max} from equation (30) into equation (35), we find that the maximum value of k_∞^2 is given by

$$(k_\infty^2)_{max} = \frac{\alpha_{max}}{1 + \alpha_{max}} = k_{31}^2 \tag{36}$$

implying that the system's coupling coefficient converges to the active material's coupling coefficient for infinitely many electrode segments and under the aforementioned α_{max} condition, as an upper limit. To demonstrate the convergence of the electromechanical coupling as the number of electrodes becomes large, consider a uniform bimorph cantilever beam with S evenly distributed electrodes, such that $x_j^L = (j-1)L/S$ and $x_j^R = jL/S$. With that assumption, k_i^2 can be calculated for each mode by comparing open- and short-circuit natural frequencies at various values of S, which is shown in figure 3. As S becomes large, the coupling approaches k_∞^2, converging more quickly for lower modes.

It is worth noting that the value of α can be effectively increased by using negative capacitance shunting [13]. This can be seen explicitly by using

$$h(s) = -cs + (1 - c)g(s), \tag{37}$$

where $g(s)$ is the normalized admittance of a shunt circuit designed in the absence of negative capacitance shunting, and $0 < c < 1$ represents the fraction of the piezoelectric capacitance being canceled. The response is then

$$H_r(s) = \frac{Q_r(s)}{s^2 + \omega_r^2\left(1 + \frac{\alpha s}{s - cs + (1-c)g(s)}\right)} \tag{38}$$

$$= \frac{Q_r(s)}{s^2 + \omega_r^2\left(1 + \frac{\alpha_{nc} s}{s + g(s)}\right)}, \tag{39}$$

where

$$\alpha_{nc} = \frac{\alpha}{1 - c} \tag{40}$$

is the effective dimensionless electromechanical coupling in the presence of negative capacitance shunting. Note that, although equation (40) suggests that α_{nc} can be made arbitrarily large, there are practical limitations preventing such designs, such as the required input power, electrical losses, and stability issues in the circuit.

4. Root locus interpretation of modal response

By rewriting equation (24), the transfer function for the rth vibration mode can be obtained as

$$\frac{H_r(s)}{Q_r(s)} = \frac{1}{s^2 + \omega_r^2\left(1 + \frac{\alpha s}{s + h(s)}\right)}. \tag{41}$$

The poles and zeros of this expression give a great deal of information about the structure's response. Zeros correspond to frequencies where a particular mode shows no response, and poles correspond to resonances of a particular mode. For this purpose, it is useful to interpret the transfer function as

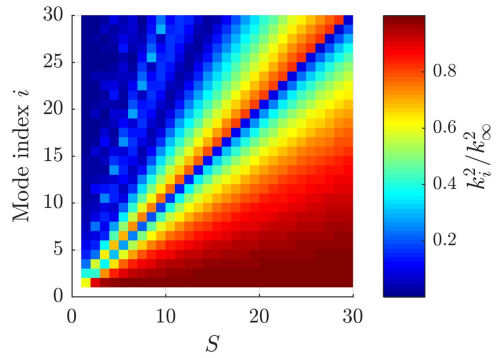

Figure 3. Modal electromechanical coupling versus number of electrode pairs on a bimorph cantilever for the *i*th mode. For sufficiently large S, k_i^2 approaches $k_\infty^2 = \alpha/(1+\alpha)$. Slope cancellation along the line $i = S$ gives very low coupling.

the closed-loop transfer function of a feedback control system, with plant and feedback transfer functions

$$G(s) = \frac{1}{s^2}, \tag{42}$$

$$F(s) = 1 + \frac{\alpha s}{s + h(s)} \tag{43}$$

with proportional gain $K = \omega_r^2$. Thus, we consider the poles and zeros of the system

$$G(s)F(s) = \frac{1}{s^2}\left(1 + \frac{\alpha s}{s + h(s)}\right) \tag{44}$$

$$= \frac{(1+\alpha)s + h(s)}{s^2(s + h(s))}. \tag{45}$$

Simply by considering the poles and zeros of this expression for a given $h(s)$, the effect of increasing ω_r^2 on the poles (resonances) of the system can be inferred using well-known root locus analysis [30]. This gives a quick way to determine where the resonances of the system are moved by the addition of the segmented shunt circuits, which makes it immediately clear if there is a bandgap present, as will be demonstrated for the simplest form of the locally resonant bandgap.

5. Estimation of electroelastic bandgap size

Although the general framework in the previous section allows the analysis of any type of linear shunt circuit, one interesting example is the locally resonant bandgap that forms from inductive shunting. To obtain the locally resonant bandgap, assume that the circuit impedance is due to an ideal (lossless) inductor, such that

$$Y_j(s) = \frac{1}{L_j s}, \qquad h(s) = \frac{\omega_t^2}{s}, \tag{46}$$

where L_j is the inductance applied to the *j*th shunt (not to be confused with the beam length L), and

$$\omega_t^2 = \frac{1}{L_j C_{p,j}}. \tag{47}$$

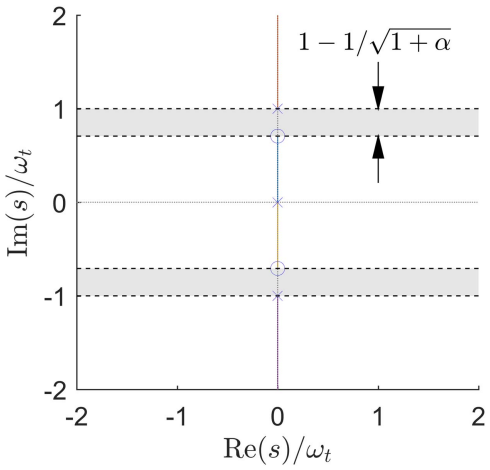

Figure 4. Root locus plot showing the bandgap for $\omega_r^2 > 0$ and $\alpha = 1$. Solid lines show the root locus, 'o' and 'x' markers show zeros and poles for $\omega_r^2 = 0$. Dashed lines and shaded regions show the frequency range of the bandgap.

Then,

$$\frac{H_r(s)}{Q_r(s)} = \frac{1}{s^2 + \omega_r^2\left(1 + \frac{\alpha s^2}{s^2 + \omega_t^2}\right)}. \tag{48}$$

Note that as $s \to j\omega_t$, $H_r(s)/Q_r(s) \to 0$, an antiresonance is present for every mode. This is the continuous system analog to a perfectly tuned vibration absorber. Using the previously mentioned root locus interpretation of the modal response, the system transfer function is

$$G(s)F(s) = \frac{(1+\alpha)s^2 + \omega_t^2}{s^2(s^2 + \omega_t^2)}. \tag{49}$$

There are zeros at $s = \pm j\omega_t/\sqrt{1+\alpha}$, poles at $s = \pm j\omega_t$, and a second order pole at $s = 0$. The corresponding root locus plot is shown in figure 4.

There can never be any poles (corresponding to resonant frequencies) in the range $\omega_t/\sqrt{1+\alpha} < \mathrm{Im}(s) < \omega_t$. Thus, the frequency range

$$\frac{\omega_t}{\sqrt{1+\alpha}} < \omega < \omega_t \tag{50}$$

defines the locally resonant bandgap when there are an infinite number of electrodes and resonant shunts. Substituting equation (46) into equation (25), assuming $s = j\omega$, the dynamic modal stiffness of the structure is given by

$$\frac{K(j\omega)}{K_{SC}} = 1 - \frac{\alpha\omega^2}{\omega_t^2 - \omega^2}. \tag{51}$$

The bandgap limits in equation (50) can be understood as the frequency range in which $K(j\omega)$ becomes negative. Far from the bandgap ($\omega \gg \omega_t$), the modal stiffness approaches $K = (1+\alpha)K_{SC}$, indicating that the stiffness is increased by a factor of $1+\alpha$, since each resonant shunt becomes like an open circuit.

Table 2. Bandgap width as a percentage of target frequency for selected piezoelectric materials (for $c_s = 69$ GPa, $\rho_s = 2700$ kg m^{-3}, $h_s = 0.1$ mm, $h_p = 0.3$ mm, $L = 100$ mm, and $b = b_e = 10$ mm).

Material	$\Delta\omega/\omega_t$ (%)
PZT-5A	7.01
PZT-5H	6.71
PZN-PT (4.5%)	11.44
PZN-PT (8%)	17.22
PMN-PT (30%)	10.83
PMN-PT (33%)	17.07
0.27PIN-0.40PMN-0.33PT	17.95

The bandwidth of vibration attenuation of the locally resonant bandgap is

$$\Delta\omega = \omega_t\left(1 - \frac{1}{\sqrt{1+\alpha}}\right). \tag{52}$$

For reference, the expected bandwidth as a percentage of the target frequency ω_t is shown in table 2 for the materials from table 1 using the same geometric parameters. Note that for both PZT-5A and PZT-5H, the bandgap is expected to be a small fraction of the target frequency, whereas some of the single crystals are approaching 20% bandwidth.

To center the bandgap at some center frequency ω_c, the target frequency should be selected as

$$\omega_t = \frac{2\omega_c\sqrt{1+\alpha}}{1+\sqrt{1+\alpha}}. \tag{53}$$

Note that, with an infinite number of electrodes, the bandgap edge frequencies have no dependence on the boundary conditions of the beam or the type of excitation. In addition, the bandgap is asymmetric about the target frequency, but in the opposite direction (i.e. below the target frequency, rather than above) as the mechanical resonator mass-based bandgap recently analyzed with a similar approach [18].

The bandwidth of the locally resonant bandgap increases if negative capacitance is used in addition to resonant shunting. Substituting equation (40) into equation (52) gives the bandgap bandwidth as

$$\Delta\omega = \omega_t\left(1 - \frac{\sqrt{1-c}}{\sqrt{1-c+\alpha}}\right). \tag{54}$$

The dimensionless bandwidth $\Delta\omega/\omega_t$, i.e. the bandwidth of the bandgap normalized by the target frequency, is shown as a function of fractional negative capacitance c in figure 5 for constant α.

A typical way to measure the response of the structure is transmissibility, defined as the ratio of displacements at some output location x_{out} to some input location x_{in}, i.e.

$$\text{TR}(\omega) = \left|\frac{w(x_{\text{out}})}{w(x_{\text{in}})}\right| = \left|\frac{\sum_{r=1}^{N}\phi_r(x_{\text{out}})H_r(j\omega)}{\sum_{r=1}^{N}\phi_r(x_{\text{in}})H_r(j\omega)}\right|. \tag{55}$$

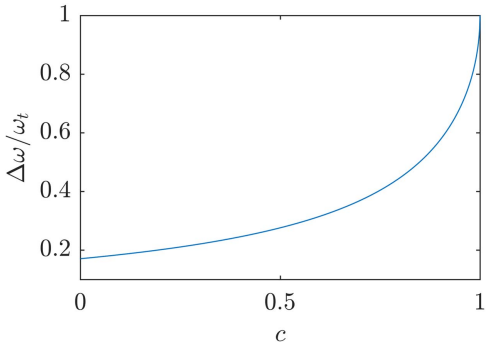

Figure 5. Dimensionless bandgap bandwidth versus fractional negative capacitance for $\alpha = 0.45$. Note that the maximum bandwidth is $\Delta\omega/\omega_t = 1$, since the upper edge frequency of the bandgap is fixed at ω_t.

With a closed form expression for $H_r(s)$, equation (55) becomes simple to evaluate for very large N. Consider the previously discussed bimorph cantilever with $c_s = 69$ GPa, $\rho_s = 2700$ kg m^{-3}, $h_s = 0.1$ mm, $h_p = 0.3$ mm, $L = 100$ mm, and $b = b_e = 10$ mm (and let PMN-PT with 33% PT be the piezoelectric material). This structure has clamped-free boundary conditions (clamped at $x = 0$ and free at $x = L$). Let the output be the transverse displacement at the tip ($x = L$). Rather than looking at a particular excitation point, the input location x_{in} can be allowed to vary along with frequency, giving a full picture of the beam's response, as shown in figure 6. The resulting bandgap in this figure agrees with the bandgap size approximation in table 2 based on equation (52).

6. Finite number of electrodes and validation of bandgap size

The simplifications in our analysis thus far rely on the assumption of an infinite number of segmented electrodes. For practical design purposes, it is necessary to understand how the system behaves with a finite number of electrode pairs and determine how many electrodes are necessary for a target frequency neighborhood. For the infinite-electrode approximation to be used in case of a finite number of electrodes, the key approximation is

$$\sum_{j=1}^{S} EI\frac{\Delta\phi'_{r,j}}{\Delta x_j}\frac{\Delta\phi'_{k,j}}{\Delta x_j}\Delta x_j \approx \int_0^L EI\frac{\mathrm{d}^2\phi_r}{\mathrm{d}x^2}\frac{\mathrm{d}^2\phi_k}{\mathrm{d}x^2}\mathrm{d}x = \omega_r^2\delta_{rk}. \tag{56}$$

Using equations (12) and (13), it is simple to obtain the structure's response and approximate natural frequencies using typical multi-degree-of-freedom dynamical systems techniques. To check the convergence to the expected infinite-electrodes behavior as $S \to \infty$, we assume that the electrodes have uniform length $\Delta x_j = L/S$, covering the entire structure, such that $x_j^L = (j-1)L/S$ and $x_j^R = jL/S$. The electrode pattern is then determined by S only, and the resonant frequencies can be obtained at each value of S. Similarly, the deformed shape of the beam under harmonic base excitation can be obtained at each S. The resulting

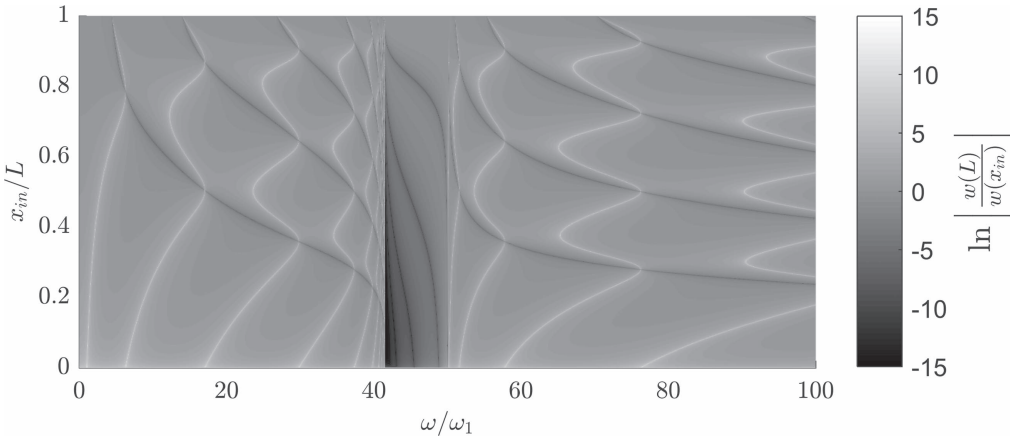

Figure 6. Tip transmissibility $|w(L)/w(x_{\text{in}})|$ versus input location and excitation frequency for a bimorph cantilever beam with a harmonic point force excitation at x_{in} bearing an infinite number of segmented electrodes, $\alpha = 0.45$ (PMN-PT 33%), $\omega_t = 50\omega_1$, $N = 300$.

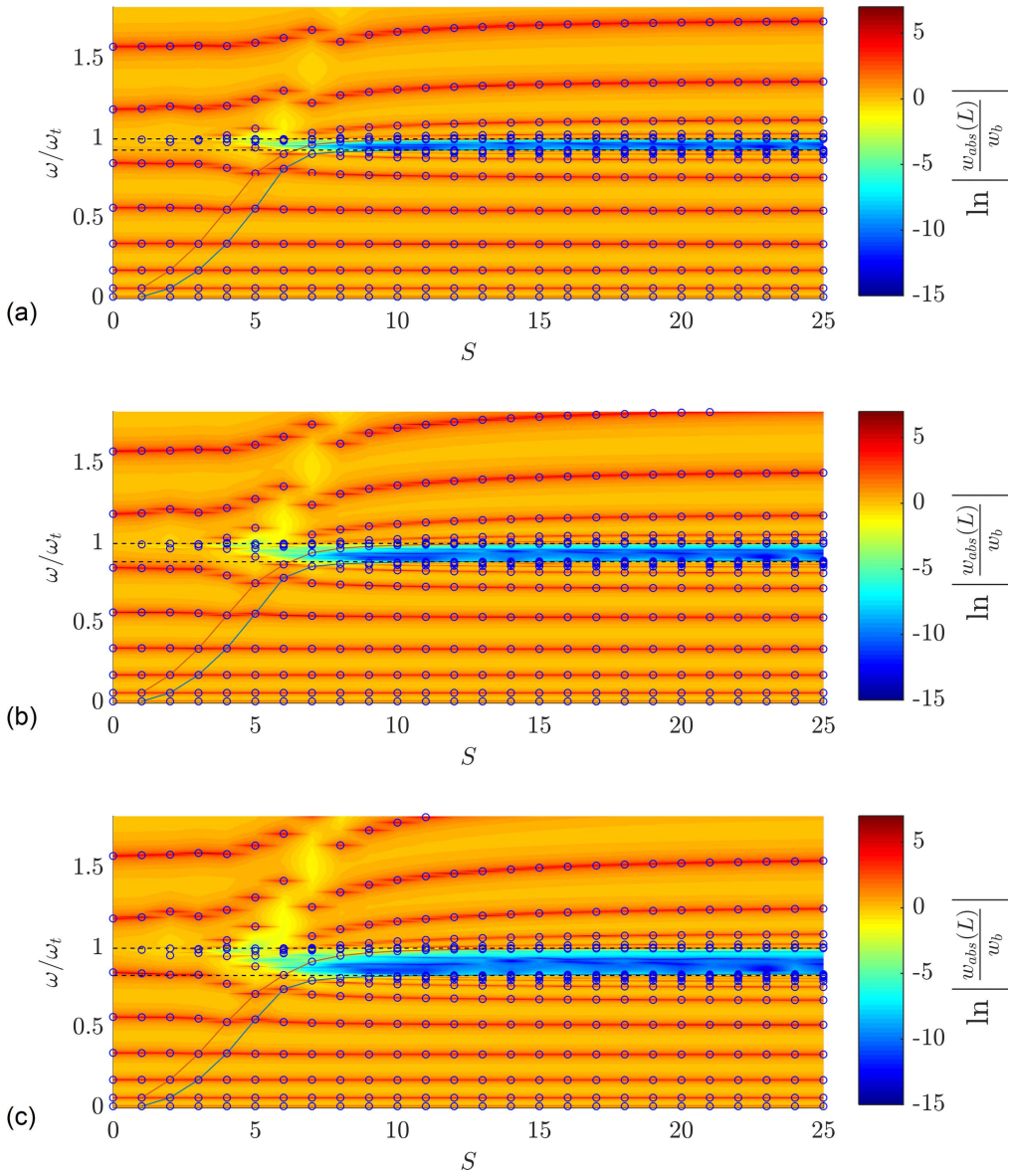

Figure 7. Transmissibility and resonant frequencies versus S for (a) PZT-5A ($\alpha = 0.16$), (b) PZN-PT (4.5%) ($\alpha = 0.27$), (c) PMN-PT (33%) ($\alpha = 0.45$) for a uniform bimorph cantilever beam excited by base motion, $\omega_t = 100\omega_1$, $N = 200$. Small circles indicate resonant frequencies, heatmap shows transmissibility, dashed lines show the expected bandgap edge frequencies from equation (50), and solid lines track ω_{S+1} and ω_S.

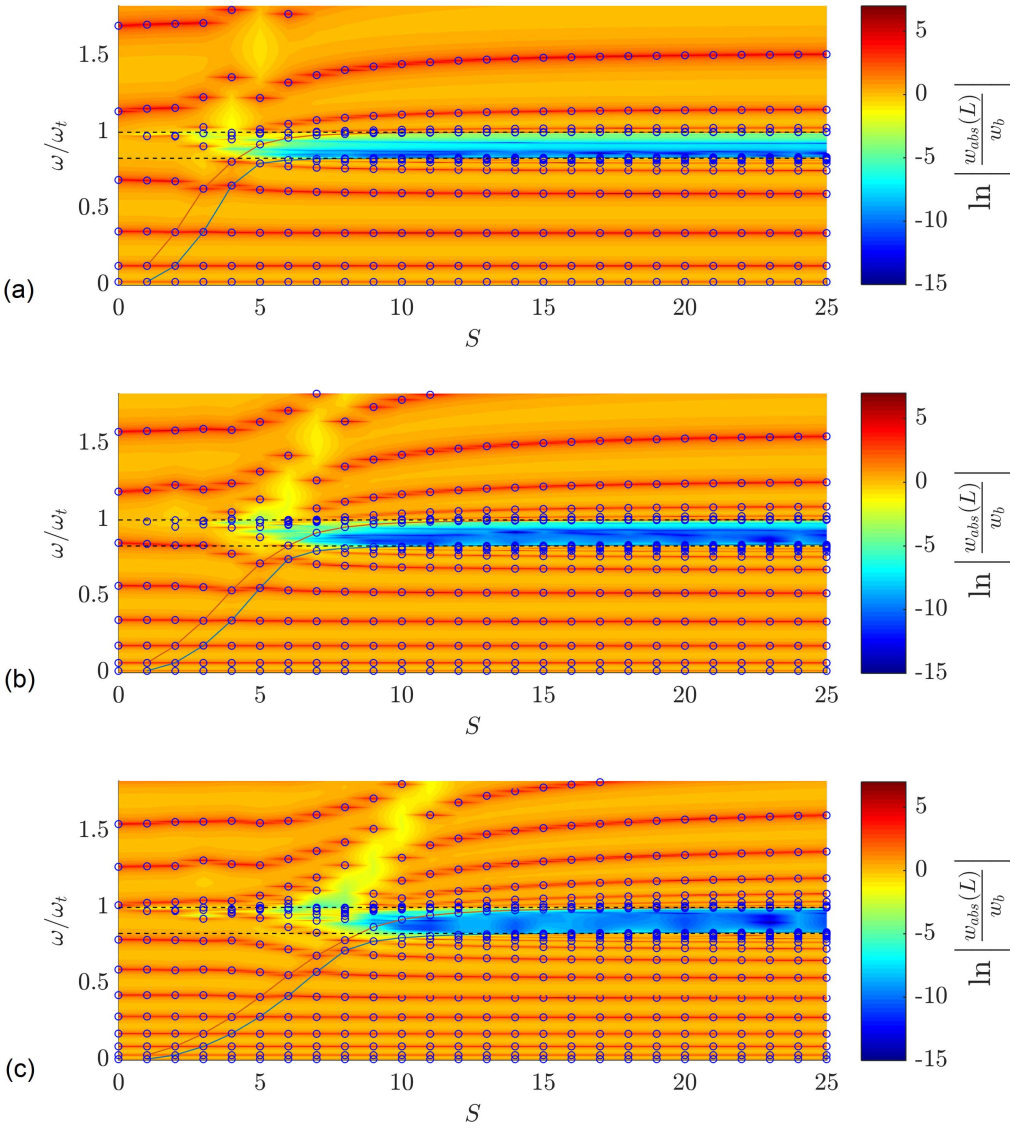

Figure 8. Transmissibility and resonant frequencies versus S for (a) $\omega_t = 50\omega_1$, (b) $\omega_t = 100\omega_1$, (c) $\omega_t = 200\omega_1$ for a uniform bimorph cantilever beam (PMN-PT 33%) excited by base motion, $\alpha = 0.45$, $N = 200$. Small circles indicate resonant frequencies, heatmap shows transmissibility, dashed lines show the expected bandgap edge frequencies from equation (50), and solid lines track ω_{S+1} and ω_S.

surface plots are shown in figure 7 for a variety of piezoelectric materials from table 1 using the previously given cantilever properties with aluminum substrate. Additionally, figure 8 shows the surface plots for various target frequencies ω_t for the same cantilever with a fixed piezoelectric material. The bandgap approximation for infinite electrodes ($S \to \infty$) based on equation (50) is shown with dashed lines and agrees with numerical simulations after sufficient number of electrodes. In all of these simulations, the bandgap is clearly indicated by sharp reduction in transmissibility. Figure 7 confirms that the bandgap width increases as α increases. The convergence to the expected bandgap in equation (50) for sufficiently large S is clear in all of the plots in figures 7 and 8, and figure 8 shows that more segmentation (larger S) is required for the bandgap to form as ω_t increases.

Although figures 7 and 8 show that some minimum amount of segmentation is necessary for the bandgap to form, it should be noted that the required inductance to achieve a certain target frequency increases as S increases. In many applications, it is likely most practical to choose the smallest value of S which allows the use of the infinite-electrode approximation for design purposes, in order to keep the required inductance at a reasonable level. On the other hand, if the transfer function of the circuit is to be simulated with op-amps or digital components [25], this may not be as much of a concern.

7. Conclusions

Elastic metastructures made from locally resonant metamaterials can exhibit bandgaps at wavelengths much longer than the lattice size for low-frequency vibration attenuation. In analogy with those mechanical metastructures, electromechanical metastructures made from elastic substrates with piezoelectric layers shunted to resonating circuits also offer

low-frequency electroelastic bandgaps. This work aimed to provide a fundamental understanding of bandgap formation in finite piezoelectric structures using a modal analysis approach, along with closed-form expressions and bandgap design insights. We presented a detailed analytical and numerical investigation of a one-dimensional locally resonant piezoelectric metastructure with segmented electrodes under transverse vibrations. The simplifying assumption of infinite electrodes was used to derive a closed form expression for the bandgap size in terms of the target frequency and a dimensionless electromechanical coupling term. It was shown that the bandgap formation in piezoelectric metastructures is associated with a frequency-dependent modal stiffness term, unlike the frequency-dependent modal mass term in mechanical metastructures. Therefore the bandgap in piezoelectric metastructures forms on the left-hand side of the target frequency (on the frequency axis) of the resonators, which is the oppostie of purely mechanical locally resonant bandgap formation. Since the bandgap size for a given geometric configuration was found to be dependent mainly on the system-level electromechanical coupling, various piezoelectric ceramics and single crystals were compared, and it was shown that single crystals (e.g. PMN-PT) provide significantly wider bandwidth as compared to ceramics (e.g. PZT-5A). Finally, numerical studies were performed to demonstrate that the closed-form bandgap expression derived in this work holds for a finite number of electrode segments. The number of electrodes required for bandgap formation increases with increased target frequency.

Acknowledgments

This work was supported by the Air Force Office of Scientific Research grant FA9550-15-1-0397 'Integrated multi-field resonant metamaterials for extreme, low frequency damping.'

References

[1] Nashif A D, Jones D I and Henderson J P 1985 *Vibration Damping* (New York: Wiley)
[2] Jones D I 2001 *Handbook of Viscoelastic Vibration Damping* (New York: Wiley)
[3] Lesieutre G A 1998 Vibration damping and control using shunted piezoelectric materials *Shock Vib. Dig.* **30** 187–95
[4] Ahmadian M and Deguilio A P 2001 Recent advances in the use of piezoceramics for vibration suppression *Shock Vib. Dig.* **33** 15–22
[5] Forward R L 1979 Electronic damping of vibrations in optical structures *Appl. Opt.* **18** 690–7
[6] Hagood N W and von Flotow A 1991 Damping of structural vibrations with piezoelectric materials and passive electrical networks *J. Sound Vib.* **146** 242–68
[7] Den Hartog J P 1956 *Mechanical Vibrations* 4th edn (New York: McGraw-Hill)
[8] Hollkamp J J 1994 Multimodal passive vibration suppression with piezoelectric materials and resonant shunts *J. Intell. Mater. Syst. Struct.* **5** 49–57
[9] Wu S 1998 Method for multiple mode shunt damping of structural vibration using a single PZT transducer *Proc. SPIE* **3327** 159–68
[10] Behrens S, Fleming A J and Moheimani S O R 2003 A broadband controller for shunt piezoelectric damping of structural vibration *Smart Mater. Struct.* **12** 18–28
[11] Park C H and Baz A 2005 Vibration control of beams with negative capacitive shunting of interdigital electrode piezoceramics *J. Vib. Control* **11** 331–46
[12] de Marneffe B and Preumont A 2008 Vibration damping with negative capacitance shunts: theory and experiment *Smart Mater. Struct.* **17** 035015
[13] Tang J and Wang K W 2001 Active-passive hybrid piezoelectric networks for vibration control: comparisons and improvement *Smart Mater. Struct.* **10** 794–806
[14] Clark W W 2000 Vibration control with state-switched piezoelectric materials *J. Intell. Mater. Syst. Struct.* **11** 263–71
[15] Corr L R and Clark W W 2002 Comparison of low-frequency piezoelectric switching shunt techniques for structural damping *Smart Mater. Struct.* **11** 370
[16] Lefeuvre E, Badel A, Petit L, Richard C and Guyomar D 2006 Semi-passive piezoelectric structural damping by synchronized switching on voltage sources *J. Intell. Mater. Syst. Struct.* **17** 653–60
[17] Liu Z, Zhang X, Mao Y, Zhu Y Y, Yang Z, Chan C T and Sheng P 2000 Locally resonant sonic materials *Science* **289** 1734–6
[18] Sugino C, Leadenham S, Ruzzene M and Erturk A 2016 On the mechanism of bandgap formation in locally resonant finite elastic metamaterials *J. Appl. Phys.* **120** 134501
[19] Casadei F, Ruzzene M, Dozio L and Cunefare K A 2010 Broadband vibration control through periodic arrays of resonant shunts: experimental investigation on plates *Smart Mater. Struct.* **19** 015002
[20] Airoldi L and Ruzzene M 2011 Design of tunable acoustic metamaterials through periodic arrays of resonant shunted piezos *New J. Phys.* **13** 113010
[21] Senesi M and Ruzzene M 2011 Piezoelectric superlattices as multi-field internally resonating metamaterials *AIP Adv.* **1** 041504
[22] Jin Y, Bonello B and Pan Y 2014 Acoustic metamaterials with piezoelectric resonant structures *J. Phys. D: Appl. Phys.* **47** 245301
[23] Bergamini A, Zundel M, Parra E, Delpero T, Ruzzene M and Ermanni P 2015 Hybrid dispersive media with controllable wave propagation: a new take on smart materials *J. Appl. Phys.* **118** 154310
[24] Erturk A and Inman D J 2009 An experimentally validated bimorph cantilever model for piezoelectric energy harvesting from base excitations *Smart Mater. Struct.* **18** 025009
[25] Fleming A J, Behrens S and Moheimani S O R 2000 Synthetic impedance for implementation of piezoelectric shunt-damping circuits *Electron. Lett.* **36** 1525–6
[26] Cao H, Schmidt V H, Zhang R, Cao W and Luo H 2004 Elastic, piezoelectric, and dielectric properties of 0.58 Pb (Mg1/3Nb2/3) O3-0.42 PbTiO3 single crystal *J. Appl. Phys.* **96** 549–54
[27] Zhang R, Jiang B, Jiang W and Cao W 2003 Complete set of properties of 0.92Pb(Zn1/3Nb2/3)O3-0.08PbTiO3 single crystal with engineered domains *Mater. Lett.* **57** 1305–8
[28] Liu X, Zhang S, Luo J, Shrout T R and Cao W 2009 Complete set of material constants of Pb(In1/2Nb1/2)O3-Pb(Mg1/3Nb2/3)O3-PbTiO3 single crystal with morphotropic phase boundary composition *J. Appl. Phys.* **106** 074112
[29] Lesieutre G A and Davis C L 1997 Can a coupling coefficient of a piezoelectric device be higher than those of its active material? *Proc. SPIE* **3041** 281–92
[30] Ogata K 2009 *Modern Control Engineering* 5th edn (Englewood Cliffs, NJ: Prentice-Hall)